Study on Shell-and-Tube Heat Exchanger Models with Different Degree of Complexity for Process Simulation and Control Design

Javier Bonilla[a,b,*], Alberto de la Calle[c], Margarita M. Rodríguez-García[a], Lidia Roca[a,b], Loreto Valenzuela[a]

[a] *CIEMAT-PSA, Centro de Investigaciones Energéticas, Medioambientales y Tecnológicas - Plataforma Solar de Almería, Almería, Spain (e-mail: javier.bonilla@psa.es, margarita.rodriguez@psa.es, lidia.roca@psa.es, loreto.valenzuela@psa.es).*
[b] *CIESOL, Solar Energy Research Center, Joint Institute University of Almería - CIEMAT, Almería, Spain*
[c] *CSIRO Energy, 10 Murray Dwyer Ct, Mayfield West, NSW 2304, Australia (e-mail: alberto.delacallealonso@csiro.au).*

Abstract

Many commercial solar thermal power plants rely on indirect thermal storage systems in order to provide a stable and reliable power supply, where the working fluid is commonly thermal oil and the storage fluid is molten salt. The thermal oil - molten salt heat exchanger control strategies, to charge and discharge the thermal storage system, strongly affect the performance of the whole plant. Shell-and-tube heat exchangers are the most common type of heat exchangers used in these facilities. With the aim of developing advanced control strategies accurate and fast dynamic models of shell-and-tube heat exchangers are essential. For this reason, several shell-and-tube heat exchanger models with different degrees of complexity have been studied, analyzed and validated against experimental data from the CIEMAT-PSA molten salt test loop for thermal energy systems facility. Simulation results are compared in steady-state as well as transient predictions in order to determine the required complexity of the model to yield accurate results.

Keywords: Multi-pass shell-and-tube heat exchanger, dynamic simulation, transient response, thermal energy storage, molten salt, Modelica.

1. Introduction

Heat exchanger modeling and simulation has been extensively addressed in the literature due to its importance in industrial applications. Many kinds of heat exchanger models have been developed targeting different aspects of interest such as, steady state and transient predictions, one-dimensional process and three-dimensional detailed models, simplified analytical models, linearized models, etc. In [1], it is presented an exhaustive review of heat exchanger models dealing with different fields of interest. Special mention deserve shell-and-tube heat exchangers for their role in process engineering, thus being these the subject of numerous publications dealing with their efficient modeling. In [2], a detailed modeling review of this kind of heat exchangers is presented.

This work focuses on the comparison and evaluation of several shell-and-tube heat exchanger models with different level of complexity and with the purpose of process simulation and control design. In both areas, not only reliable and accurate but also fast heat exchanger models are required.

The simulation results from these models have been compared against experimental data from a multi-pass shell-and-tube heat exchanger. This heat exchanger is part of the CIEMAT-PSA molten salt test loop for thermal energy systems (MOSA) facil-

*Corresponding author

Figure 1: CIEMAT-PSA MOSA facility

ity, a facility with the aim of studying Thermal Energy Storage (TES) systems in solar thermal power plants.

Many factors such as, environmental issues and concerns about sustainability are presently encouraging investment and research into alternative sources that might provide renewable, clean, sustainable and efficient energy. Solar thermal power plants are appropriate for large-scale energy production due to their dispatchability on demand, since they efficiently store heat in TES systems. Therefore, many commercial solar thermal power plants rely on TES systems to provide a stable and reliable power supply [3, 4, 5].

The performance of solar thermal power plants with TES systems is highly influenced by the heat exchanger control strategies applied in the charging and discharging processes [6]. Therefore, advanced control strategies may improve the performance of the whole plant. Accurate and fast dynamic plant models are required in order to design and test control strategies. For this reason, the heat exchanger model is an important part in the design, testing and validating of advanced control strategies for TES systems in solar thermal power plants.

This paper is organized as follows, section 2 introduces the experimental plant and the heat exchanger under consideration, section 3 describes the different heat exchanger models considered in this work, section 4 presents simulation results from several heat exchanger models against experimental data at design conditions, steady-state and transient predictions. Finally, section 5 draws the main conclusions and summarizes future work.

Figure 2: Two-unit multi-pass shell-and-tube heat exchanger

2. Experimental Plant: CIEMAT-PSA MOSA Facility

A molten salt testing facility was set up at Plataforma Solar de Almería (PSA), division of CIEMAT, the public research center for Energy, Environmental and Technological Research, which is owned by the Spanish government. The aim of this facility is to study TES systems, evaluate and control the heat exchange between the molten salt and different kinds of potential heat transfer fluid in solar thermal power plants (i.e. thermal oil and pressurized gases). In order to study pressurized gases, the MOSA facility is coupled to the innovative fluids test loop facility [7] by means of a CO_2 - molten salt heat exchanger. This last facility comprises two parabolic-trough collectors.

The main components of the MOSA facility (figure 1) are briefly described in the following list. Consult [8] and [9] for further details.

- *Molten salt tanks.* Hot and cold molten salt tanks reproduce the sensible-heat TES systems

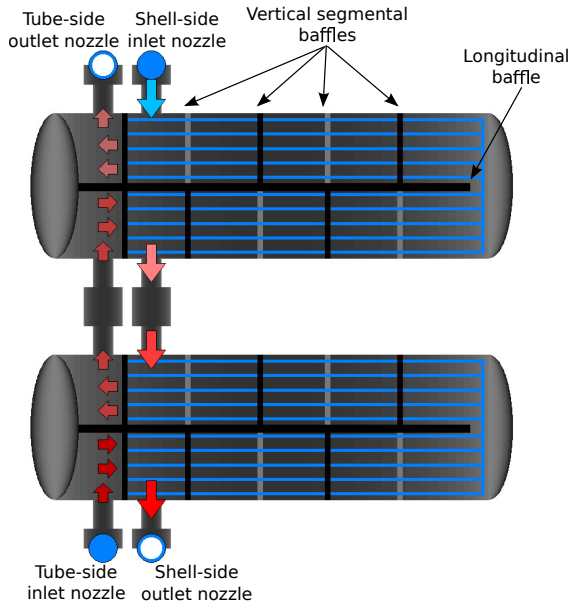

Figure 3: Heat exchanger schematic representation [10]

of commercial solar power plants. The hot tank is at the ground level whereas the cold tank is under ground level.

- *Molten salt air cooler.* This air cooler replicates the molten salt discharging process by cooling down the molten salt.
- *CO_2 - molten salt heat exchanger.* This heat exchanger allows exchanging heat from pressurized gases from the innovative fluids test loop facility.
- *Two flanged pipe sections.* Components can be installed in the two flanged pipe sections in order to be tested in the molten salt circuit under real working conditions.
- *Electrical heat-tracing system.* Its purpose is to prevent salt freezing.
- *Thermal oil loop.* It allows storing and releasing thermal energy to/from the molten salt. This loop includes the following components: a thermal oil expansion tank, a centrifugal pump, an oil heater, a thermal oil - molten salt heat exchanger, thermal oil air cooler, an expansion tank and nitrogen bottles to render the molten salt and thermal oil inert. The purpose of the oil heater is to provide the same amount of heat than parabolic-trough collectors. Therefore, the oil heater can be used to emulate them and replicate transients such as, start-ups, shutdowns and cloud disturbances.

The multipurpose MOSA facility is flexible and can work in four different operating modes, they are summarized as follows. Further details about operating modes can be consulted in [9].

- *Mode 1.* In this mode, energy coming from the innovative fluids test loop is used to charge the molten salt TES system.
- *Mode 2.* The molten salt is cooled down by means of the air cooler system in this mode.
- *Mode 3.* In mode 3, the TES system is charged from thermal energy of the thermal oil loop by means of the thermal oil - molten salt heat exchanger.
- *Mode 4.* This mode discharges the TES system and thus heating up thermal oil by means of the same heat exchanger than in mode 3.

2.1. Two-unit Multi-Pass Shell-and-Tube Heat Exchanger

This work focuses on the modeling of the thermal oil loop heat exchanger. This heat exchanger is composed of two counter-flow multi-pass shell-and-tube

Table 1: Heat exchanger nominal conditions in mode 3

Feature	Shell side	Tube side
Fluid	Solar salt	VP-1
Inlet mass flow (kg/s)	2.08	1.57
Inlet pressure (bar)	2	14
Outlet pressure (bar)	1.6	13.97
Inlet temperature (°C)	290	380
Outlet temperature (°C)	373	313

Table 2: Heat exchanger design parameters

Design parameter	Value
Area of heat transfer	$83.02\,\mathrm{m}^2$
Mean heat transfer coef.	$238.5\,\mathrm{W/(m^2\,K)}$
Tube-side volume	$0.111\,\mathrm{m}^3$
Shell-side volume	$0.255\,\mathrm{m}^3$
Tubes per shell pass	153
Tube outer diameter	12.7 mm
Tube inner diameter	12.5 mm
Tube length per shell pass	3.4 m
Shell-side passes per unit	2
Ttube-side passes per unit	2
Baffles per shell pass	39
Baffle spacing	80 cm
Last baffle spacing	90 cm
Baffle cut	17.35 %

units, see figure 2 for a real picture of the system and figure 3 for a schematic representation. The shell-side fluid is molten salt, solar salt in particular (60 % $NaNO_3$ and 40 % KNO_3) whereas the tube-side fluid, due to its high pressure, is the commercial Therminol VP-1 thermal oil, see table 1 for nominal operating conditions.

Each unit of the heat exchanger was designed following a Tubular Exchanger Manufacturers Association (TEMA) design, in paticular a N-type front end stationary head, F-type shell and U-type rear end stationary head (NFU) design. Both units are tilted 2° in order to facilitate their drainage. The F-type shell has two shell passes defined by a longitudinal baffle as well as two tube passes in U shape (see figure 3). The F-type shell is the most common and economical heat exchanger design used at commercial parabolic-trough solar thermal power plants [11]. Thirty-nine vertical segmental baffles per shell pass, with 17.35 % vertical baffle cuts (see figure 4), force the shell-side fluid to follow a S-shaped path (see figure 5) in order to increase the convective heat transfer coefficient which has its highest value in cross flow. In counter flow (see figure 3), the tube-side fluid enters the inlet nozzle, flows along the tube bundle turning around due to the longitudinal baffle and the U-tube design, finally leaving the heat exchanger through the outlet nozzle. Consult table 2 to obtain information about the main design parameters of the heat exchanger.

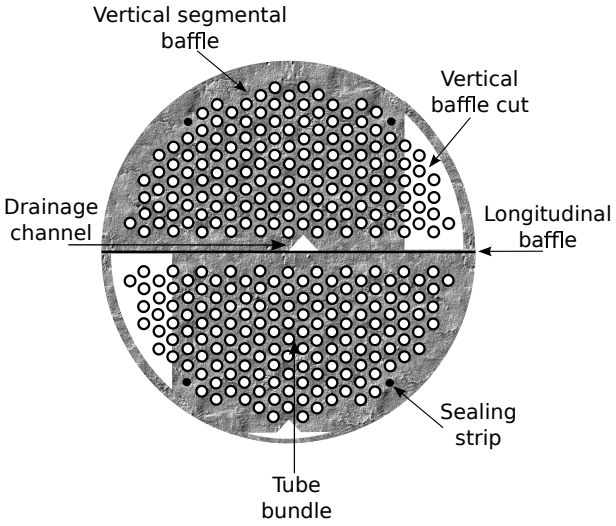

Figure 4: Heat exchanger unit cross-sectional area [10]

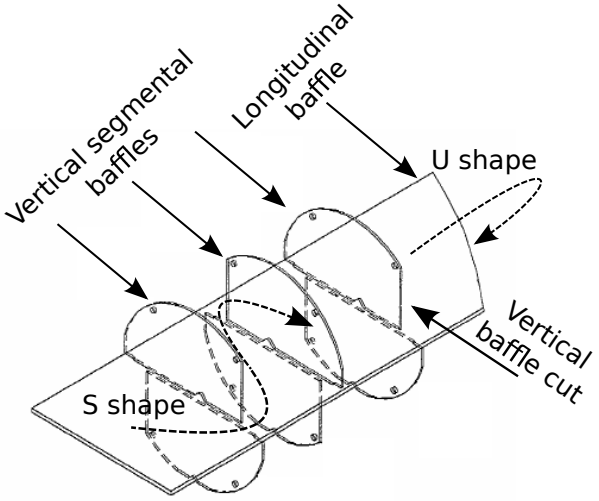

Figure 5: Heat exchanger unit cross-sectional area [10]

3. Shell-and-Tube Heat Exchanger Models with Different Degree of Complexity

Several heat exchanger models have been studied and analyzed. General assumptions considered in all the models are summarized in the following list.

- Heat conduction and radiation are negligible in the fluids. Axial heat flow is also negligible in both fluids.
- Thermal conductivity in the tube walls is infinite in normal direction of flow and zero in flow direction.
- The thermal capacitance of the heat exchanger shell is neglected.
- One-dimensional treatment in the direction of flow.

The Modelica language [12] has been used for the modeling of the heat exchanger. Modelica was developed and is maintained by the Modelica Association, a non-profit and non-governmental international association. This modeling language has been designed to model conveniently complex physical systems because the language supports the object-oriented and equation-based paradigms.

Any medium model from the Modelica Media library [13], or new implemented models which takes into account this library interface, can be used to calculate the fluid thermodynamic properties in the shell side as well as in the tube side. Both thermodynamic property mediums have been implemented in Modelica because they are not available in the Modelica Media library. Solar salt has been implemented according to the thermodynamic properties available in [14, 15] and Therminol VP-1 thermodynamic properties according to [16]. Both fluids depend only on temperature.

The studied models are listed as follows, they are explained in the following subsections. Nomenclature is shown in table 3.

- Quasi-Steady-state model (QSS model).
- Dynamic model (DY model).
- Dynamic with Thermal Capacitance Model (DYTC model).
- Dynamic with Thermal Capacitance and Cell Method Model (DYCM model).

3.1. Quasi-Steady-state Model (QSS model)

The Quasi-Steady-state (QSS) model is the easiest heat exchanger model. It is an algebraic model centered on a specific operating point for general counter-flow heat exchangers. It is based on the mathematical development presented in [17]. This model simplifies the heat exchanger considering it as a concentric tube system where the fluids flow in opposite directions while transferring sensible heat. It is a lumped parameter model which assumes that locally every state at the heat exchanger is a steady-state. The main particular assumptions, besides those stated in section 3, are the following.

- Thermal capacitance of the tube bundle metal structure has been neglected.
- Fluid friction against shell and tube walls is neglected. There is neither pressure drop at the shell side nor the tube side of the heat exchanger.
- Fluid incomprehensibility is assumed. Fluid mass storage at the heat exchanger is neglected, thus inlet and outlet mass ow rate are equal.
- Uniform thermodynamic properties are assumed. Specific heat capacities are evaluated at the mean temperature between inlet and outlet temperatures.

In order to break the algebraic loop between the inlet and outlet temperatures and to prevent zero mass flow rate, eqs. 1 and 2 are considered.

$$T_{tb,out} = T_{tb,in} - \eta_{tb}(T_{tb,in} - T_{sh,in}), \quad (1)$$

$$T_{sh,out} = T_{sh,in} + \eta_{sh}(T_{tb,in} - T_{tb,out}), \quad (2)$$

where η_{tb} and η_{sh} are two dimensionless factors whose values are non-zero when the mass flow rates ($\dot{m}_{tb}$ and $\dot{m}_{sh}$) have positive values. They are calculated by eqs. 3 and 4.

Table 3: Nomenclature

Latin letters			
Var	Description		Units
A	Surface area		[m^2]
C	Heat capacity		[J/K]
c_p	Specific heat capacity		[J/(kg K)]
d	Diameter		[m]
D	Characteristic dimension		[m]
f	Friction factor		[-]
G	Mass velocity		[kg/(m^2 s)]
$\dot{H}$	Enthalpy flow rate		[W]
j	Colburn j factor		[-]
K	Thermal conductivity		[W/(m K)]
l	Length		[m]
m	Mass		[kg]
$\dot{m}$	Mass flow rate		[kg/s]
n	Number		[-]
Nu	Nusselt number		[-]
p	Pressure		[Pa]
Pr	Prandtl number		[-]
$\dot{Q}$	Heat flow rate		[W]
Re	Reynolds number		[-]
T	Temperature		[K]
t	Time		[s]
U	Internal Energy		[J]
Greek letters			
Var.	Description		Units
α	Heat transfer coefficient		[W/(m^2 K)]
η	Dimensionless factor		[-]
θ	Dimensionless factor		[-]
Subs.	Description	Subs.	Description
amb	Ambient	av	Average
b	Baffle	he	Heat exchanger
in	Inlet	$loss$	Thermal losses
pa	Pass	out	Outlet
sh	Shell side	tb	Tube side
w	Wall		

$$\eta_{tb} = \frac{1 - e^{\theta_{he}}}{1 - \frac{\dot{m}_{tb} c_{p,tb}}{\dot{m}_{sh} c_{p,sh}} e^{\theta_{he}}}, \tag{3}$$

$$\eta_{sh} = \frac{\dot{m}_{tb} c_{p,tb}}{\dot{m}_{sh} c_{p,sh}}. \tag{4}$$

The dimensionless factor (θ_{he}) is calculated as follows,

$$\theta_{he} = \alpha_{he} A_w \left(\frac{1}{\dot{m}_{tb} c_{p,tb}} - \frac{1}{\dot{m}_{sh} c_{p,sh}} \right), \tag{5}$$

where the overall heat transfer coefficient (α_{he}) can be calculated by eq. 6.

$$\frac{1}{\alpha_{he}} = \frac{1}{\alpha_{sh}} + \frac{1}{\alpha_{tb}}. \tag{6}$$

If the thermal capacitance of the tube walls is high, the model cannot capture the transient behavior of the system. Furthermore, this model neglects the fluids mass storage in the heat exchanger, and therefore their thermal capacitance. Eqs. 1 and 4 do not consider heat losses between the shell-side fluid and the environment. However, thermal losses can be included in the model by means of the following mathematical reformulation. Heat losses are assumed as a fictitious mass flow rate ($\dot{m}_{sh,loss}$) with the same thermodynamic properties as the shell-side fluid. This mass flow rate is added to the total mass flow rate to properly calculate the temperature.

$$\dot{m}_{sh} = \dot{m}_{sh,in} + \dot{m}_{sh,loss}. \tag{7}$$

In order to assure a correct energy balance, this mass flow rate is calculated by eq. 8.

$$\dot{m}_{sh,loss} = \frac{\alpha_{loss} A_{amb}}{c_{p,sh}} \left(\frac{T_{sh,av} - T_{amb}}{T_{sh,out} - T_{sh,in}} \right), \tag{8}$$

where heat losses are calculated by Newton's law of cooling between the ambient temperature (T_{amb}), and the average shell temperature ($T_{sh,av} = (T_{sh,in} + T_{sh,out})/2$). Heat transfer coefficients (α_{sh}, α_{tb} and α_{loss}) are values that need to be calibrated with experimental data.

3.2. Dynamic Model (DY model)

The Dynamic (DY) model described in this section was developed considering that in [18]. Same assumptions than those presented in the QSS model hold for this model, besides fluid mass storage at the heat exchanger which is taken into account in the

DY model. This is a dynamic distributed parameter model, where each cell or Control Volume (CV) is a small lumped parameter counter-flow heat exchanger model. Therefore, eqs. 9 and 10 represent the energy balance for the tube side and the shell side respectively in each cell of the DY model.

$$C_{tb}\frac{dT_{tb,out}}{dt} = \dot{m}_{tb}c_{p,tb}(T_{tb,in} - T_{tb,out}) + \dot{Q}_{tb}, \quad (9)$$

$$C_{sh}\frac{dT_{sh,out}}{dt} = \dot{m}_{sh}c_{p,sh}(T_{sh,in} - T_{sh,out}) + \dot{Q}_{sh}, \quad (10)$$

where heat capacities are defined by eqs. 11 and 12. Masses depend on volumes, which as constant values, and densities which depend on the mean temperature of the CVs. Specific heat capacities also depend on the mean temperature of CVs.

$$C_{tb} = m_{tb}c_{p,tb}, \quad (11)$$

$$C_{sh} = m_{sh}c_{p,sh}. \quad (12)$$

Heat flow rates are defined by eqs. 13 and 14,

$$\dot{Q}_{tb} = \alpha_{he}A_w(T_{sh,out} - T_{tb,out}), \quad (13)$$

$$\dot{Q}_{sh} = \alpha_{he}A_w(T_{tb,out} - T_{sh,out}) - \dot{Q}_{loss}, \quad (14)$$

where the overall heat transfer coefficient (α_{he}) can be calculated by eq. 6 and thermal losses by eq. 15.

$$\dot{Q}_{loss} = \alpha_{loss}A_{amb}(T_{sh,out} - T_{amb}). \quad (15)$$

Heat transfer coefficients (α_{sh}, α_{tb} and α_{loss}) are values that need to be calibrate with experimental data.

3.3. Dynamic with Thermal Capacitance Model (DYTC model)

The Dynamic with thermal capacitance (DYTC) model is an extension of the DY model considering the heat capacity of the tube bundle metallic parts, therefore assuming that the wall temperature is the average value between the tube-side and shell-side fluid temperatures in each cell ($T_w = (T_{sh,out} + T_{tb,out})/2$), the tube-side and shell-side heat capacities can be then reformulated according to eqs. 16 and 17.

$$C_{tb} = m_{tb}c_{p,tb} + \frac{1}{2}m_w c_{p,w}, \quad (16)$$

$$C_{sh} = m_{sh}c_{p,sh} + \frac{1}{2}m_w c_{p,w}, \quad (17)$$

where the masses and specific heat capacities are parameters of the model.

3.4. Dynamic with Thermal Capacitance and Cell Method Model (DYCM model)

The Dynamic with thermal capacitance and cell method (DYCM) model has been developed following an object-oriented methodology based on first principles. A preliminary version of this model was presented in [10], some extensions have been introduced with respect to this preliminary version. One of them is heat losses to the environment and the others are more detailed shell and tube models considering the cell method introduced in [18].

The Modelica icon of this model is shown in figure 3, whereas the component diagram can be seen in figure 6. This diagram shows that each component has been modeled independently (shell, tube bundle, tube bundle walls and convection processes). The model considers the fluids flow in the tube side, as well as, in the shell side and convective heat transfer processes between the tube-side fluid, the tube bundle walls, the shell-side fluid and the ambient. Exchange of information between components is performed by means of connectors. Round connectors exchange information about fluids (mass flow rate, pressure, specific enthalpy and mass fraction, the last one is optional), whereas square connectors exchange information about heat (temperature and heat flow rate). The main components of the model are described in the following paragraphs.

3.4.1. Convection model.

Newton's law of cooling has been considered to model the convective heat transfer. The heat transfer coefficient can be dynamically calculated from any

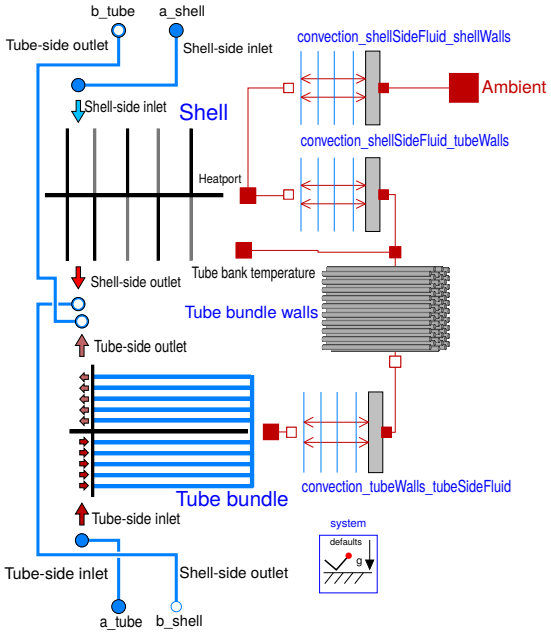

Figure 6: Heat exchanger Modelica component diagram

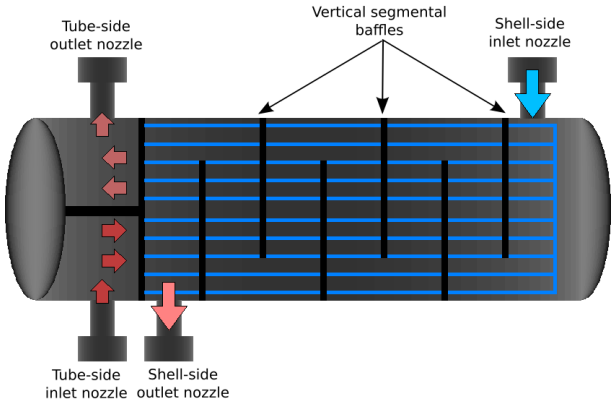

Figure 7: TEMA E-type shell heat exchanger (lateral view)

correlation implemented in the model. Convection model components can be seen in figure 6: heat transfer from the tube-side fluid to inner tube walls (*convection_tubeWalls_tubeSideFluid* component), heat transfer from outer tube walls to the shell-side fluid (*convection_shellSideFluid_tubeWalls* component) and heat transfer from shell-side fluid to the environment (*convection_shellSideFluid_shellWalls* component). Heat transfer coefficients (α_{sh}, α_{tb} and α_{loss}) are values that must be calibrated for the particular heat exchanger under consideration.

3.4.2. Tube bundle wall model.

This model is shown in figure 6 as the *tube bundle walls* component. It is discretized in CVs, the energy balance is modeled in each one of them according to eq. 18. The number of parallel tubes is a parameter of the model. Density and specific heat capacity values can be configured as average constant values or interpolated values as function of wall temperature.

$$m_w c_{p,w} \frac{dT_w}{dt} = \dot{Q}_w. \tag{18}$$

3.4.3. Shell model.

The *shell* component in figure 6 belongs to this class. Shell volume and dimensions have been modeled according to manufacturer data (see table 2). The flow of the shell-side fluid has been discretized in CVs where the one-dimensional dynamic mass (eq. 19), dynamic energy (eq. 20) and static momentum (eq. 21) balance equations have been considered. These equations apply for each CV in the model. Mass and energy balance equations have been discretized according to the Finite Volume Method (FVM) [19], whereas the static momentum balance equation is lumped in a global equation for the whole shell. Therefore, pressure drop is equally distributed among the CVs in the shell model. Pressure drop is calculated according to [20, 21], where pressure drop at cross-flow and window sections, as well as pressure drop at the inlet and outlet nozzles, for shell-and-tube heat exchangers with segmental baffles, are taken into account.

$$\frac{dm_{sh}}{dt} = \dot{m}_{sh,in} - \dot{m}_{sh,out}, \tag{19}$$

$$\frac{dU_{sh}}{dt} = \dot{H}_{sh,in} - \dot{H}_{sh,out} + \dot{Q}_{sh}, \tag{20}$$

$$\Delta p_{sh} = p_{sh,in} - p_{sh,out}. \tag{21}$$

This model has been extended with respect to

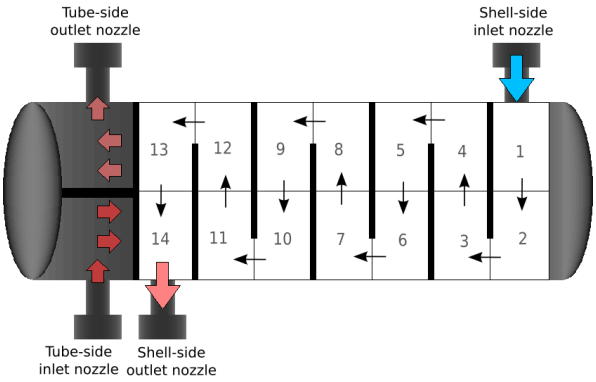

Figure 8: Cell method in the shell side of a E-type shell heat exchanger (lateral view)

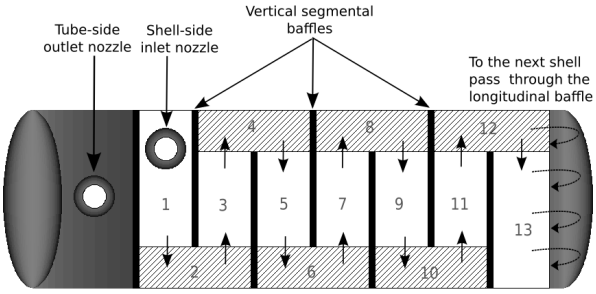

Figure 9: Cell method in the shell side of a F-type shell heat exchanger (upper view)

the one presented in [10] by considering the cell method introduced in [18]. Such work focused in heat exchangers with TEMA E-type shell configurations (one shell pass). Figure 7 shows a lateral view of a E-type shell heat exchanger with 6 vertical segmental baffles and 2 tube passes. The shell is divided in cells to account for the different flow patterns by means of linking the cells to represent the flow of the shell-side fluid. The number of shell cells is the number of baffles plus one multiplied by the number of tube passes, see figure 8.

The same idea can be applied to F-type shells, as presented in [2]. Therefore, this approach was considered in the present model. In [2], the cell method was applied to each shell pass. Note that there are 2 shell passes due to the longitudinal baffle (see figure 3). Additionally, two different kinds of cells with different flow conditions where defined in that work: window and cross-flow cells. In window cells, the shell fluid flows in counter flow with respect to the tube-side fluid, whereas it flows in cross flow in the other kind of cells. Figure 9 shows the cell distribution, where window and cross-flows cells can be seen. Window cells have a diagonal line pattern background. Note that this is an upper view of the heat exchanger and only one shell pass is represented in this figure.

3.4.4. Tube bundle model.

The *tube bundle* component in figure 6 belongs to this class. The flow of the fluid in a single tube of the tube bundle has been modeled as in the shell model, i.e. considering the one-dimensional dynamic mass (eq. 19), dynamic energy (eq. 20) and static momentum (eq. 21) balance equations. Only one tube is modeled per CV or cell, and then mass and heat flow rates are scaled considering the number of parallel tubes in each particular cell.

Pressure drop in the tube bundle has been modeled considering all the possible cases in the Moody diagram [22] using a model available in the Modelica Fluid library [13]. Pressure drop at nozzles has been calculated according to [21], whereas pressure drop in the U-shaped elbows turned out to be small and has been neglected.

As in the shell model, the tube bundle model has been extended with respect to the one presented in [10] by considering the cell method. In [18], the cell method was applied to a E-type shell heat exchanger (many tube passes). Figure 10 shows a lateral view of a E-type shell heat exchanger with two tube passes, where the tube bundle is divided in cells in order to be linked to shell cells (see figure 8) and to establish heat exchange between them.

In [2], the same method was applied to a F-type shell heat exchanger and this variant was applied in this model. Figure 11 shows the upper view of a F-type shell heat exchanger where only one tube pass is represented. Segmental vertical baffles are included in Figure 11 although they do not influence the tube-side fluid flows. Three different flow cells are defined

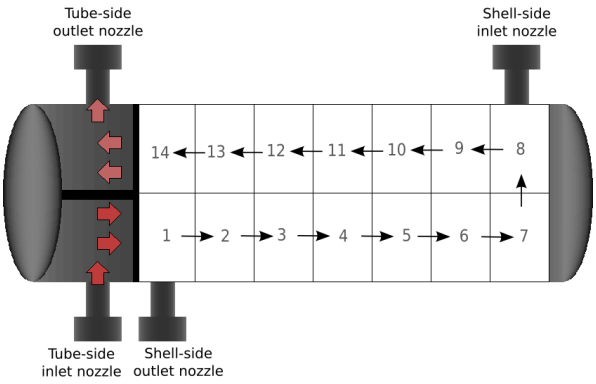

Figure 10: Cell method in the tube side of a E-type shell heat exchanger (lateral view)

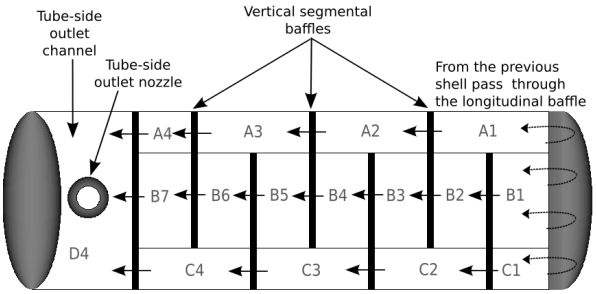

Figure 11: Cell method in the tube side of a F-type shell heat exchanger (upper view)

(A,B and C cells) in parallel. The cell numbers denote the flow order in this representation. In each one of the flow cells, one tube is considered and therefore heat flow rates are scaled as a function of the number of parallel tubes in the tube bundle. Additionally, the tube-side inlet and outlet channels in each unit are taken into account in the model (D cells). They dispatch or gather the tube-side fluid to or from the tubes in the tube bundle.

In [18], the number of cells was the number of baffles plus one multiply by the number of tube passes for a TEMA E-type shell heat exchanger. Considering an object-oriented modeling approach it is not required that the number of shell cells would be the same as the number of tube cells, since using heat ports multiple cells can be linked. This is the case for shell cells 1 and 13 (see figure 9), shell cell 1 is connected with tube cells A4 and B7, and shell cell 13 is connected with tube cells B1 and C1 (see figure 11).

For F-type shell heat exchangers, the number of shell and tube cells are given by eqs. 22 and 23, respectively, where n_b is the number of baffles and n_{pa} the number of shell or tube passes which in a F-type shell are the same.

$$n_{sh} = n_{pa}(2n_b + 1), \tag{22}$$

$$n_{tb} = n_{pa}(2n_b + 3). \tag{23}$$

Therefore, in our case that could make 158 shell CVs and 162 tube CVs, since the studied heat exchanger has 39 baffles per unit with two passes per unit. If we consider the remaining components in figure 6 (tube bundle walls and convection components) and their 158 CVs per component, that could make a total of 952 CVs. In order to reduce the time required for the simulation, the number of CVs has been reduced. Section 4.1 shows an study on the impact of the reduction in the number of CVs with respect to the simulation results.

4. Simulation, Calibration and Validation Against Experimental Data

This section concerns with the simulation of the different heat exchanger models. Section 4.1 studies the influence of the number of CVs with respect to simulation results in the DYCM model. In order to verify the models, design performance calculations provided by the manufacturer were compared to simulation results at design conditions in section 4.2. Thermocouple measurement uncertainties are presented in section 4.3. After that, some values and parameters of the models were calibrated in section 4.4 according to data from experimental campaigns. Once the models were calibrated, simulations results were validated against experimental data in section 4.5 in steady state and at several transient responses to check the model performances under a wide range of operating conditions.

Dymola [23] is the tool used for the Modelica implementations and simulations. The numerical solver used for the dynamic simulations has been DASSL [24], a variable-step variable-order multistep solver in the numerical integration of differential algebraic equation systems, where the Newton iteration method is used to solve the resulting nonlinear algebraic system of equations at each time step. The absolute and relative tolerances were set to 10^{-4}.

In order to perform the heat exchanger simulations, the following inputs must be provided to the models, as shown in figure 12.

- Tube-side and shell-side inlet mass flow rates ($\dot{m}_{tb,in}$, $\dot{m}_{sh,in}$).
- Tube-side and shell-side inlet fluid temperatures ($T_{tb,in}$, $T_{sh,in}$).
- Tube-side and shell-side outlet pressures ($\dot{p}_{tb,out}$, $\dot{p}_{sh,out}$).
- Ambient temperature (T_{amb}).

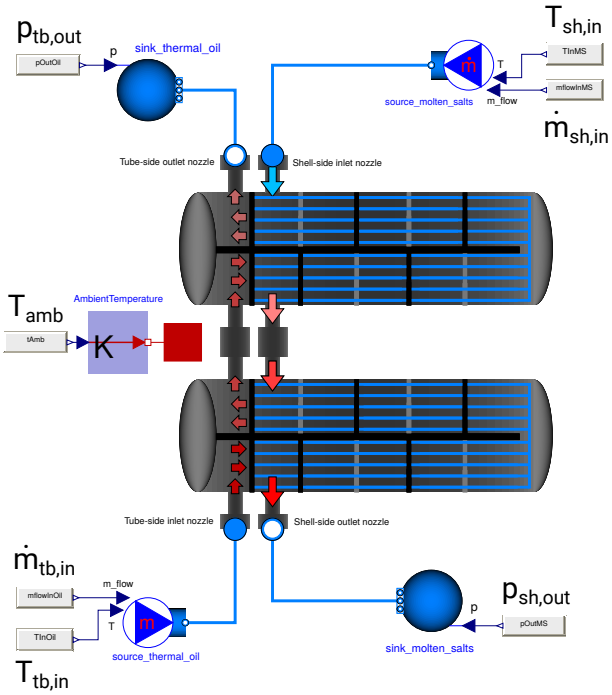

Figure 12: Heat exchanger model inputs

4.1. Level of Discretization

In this section, the DYCM model is simulated considering different numbers of CVs in order to study its convergence. Nominal operating conditions have been taken into account in the simulation according to table 1. The mean overall heat transfer coefficient has been set according to the heat exchanger design parameters (see table 2). The tube-side and shell-side heat transfer coefficients have been calculated considering eq. 6 and assuming that both coefficients have the same value.

With the aim of studying the convergence not only in steady-state but also in transients, the initial temperature of the whole heat exchanger was set to 290 °C. Table 4 shows molten salt and thermal oil outlet temperatures in steady state, differences with respect to the most detailed model (158 CVs) and execution times (compilation plus simulation times) for different cases. The number of CVs refers to the shell component.

From these results a good compromise between accuracy and execution time would be 50 CVs since the error committed is negligible (0.12 °C) with respect to the most detailed model while being close to four times faster. Execution times are low in this simulation since it is a simple step response. However, when considering more complex simulations, the simulation time is a factor than must be taken into account.

4.2. Design Conditions

All the models at nominal operating conditions (see table 1) have been compared in this section in the same terms as in the simulation performed in section 4.1. The DYCM model has been discretized in 50 CVs, whereas the DY and DYTC models consider 160 CVs, according to the formula given in [18] (see section 3.4.4) for the given number of baffles, tubes passes and units. Figures 13 and 14 show the molten salt and thermal oil outlet temperatures for the different models and also includes the nominal operating conditions provided by the manufacturer. Table 5

Table 4: Level of discretization

CVs	Temp. (°C)		Diff. (°C)		Execution time (s)
	MS	Oil	MS	Oil	
158	370.20	315.18	-	-	40.10
110	370.18	315.19	0.02	0.01	22.12
90	370.15	315.19	0.05	0.01	18.46
50	370.08	315.19	0.12	0.01	10.73
30	369.97	315.22	0.23	0.04	7.34
10	369.20	315.65	1.00	0.47	4.70

shows molten salt and thermal oil outlet temperatures in steady state and execution times for all the models plus manufacturer design conditions.

The simple algebraic QSS model provides a good approximation. The DY and DYTC models predict higher molten salt outlet temperatures than the DYCM model since they assume a pure counter-flow heat exchanger whereas the DYCM model considers two different flow sections: cross-flow and window sections, and a more precise approximation in theory with respect to the remaining models and the manufacturer calculations.

The effect of the tube bundle thermal capacitance in the DYTC model with respect to the DY model can be clearly seen in Figure 14 in the initial temperature change from 290 °C to nominal operating temperature.

Table 5: Design conditions

Model	Temperature (°C)		Execution time (s)
	MS	Oil	
Manufacturer	373.00	313.00	-
QSS	374.18	315.06	2.60
DY	373.20	312.58	16.67
DYTC	373.20	312.57	16.70
DYCM	370.08	315.19	10.73

4.3. Thermocouple meausurement uncertainties

According to the International Electrotechnical Commission (IEC) 584.3 norm, the allowable manufacturing tolerance of the K-type class 2 thermocouples is up to 3 °C. However, the thermocouples

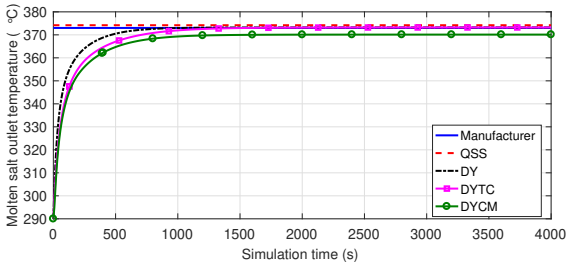

Figure 13: Molten salt outlet temperature from different models at design conditions

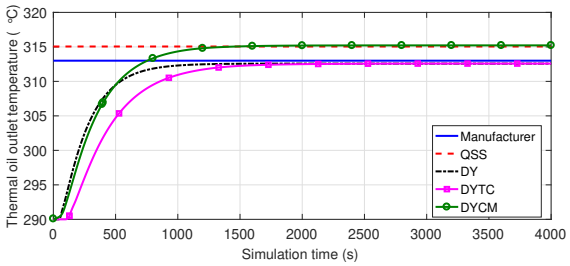

Figure 14: Thermal oil outlet temperature from different models at design conditions

in the facility were calibrated with respect to a digital thermometer in a temperature dry-well calibrator. With the aim of fitting thermocouple temperatures to the digital thermometer temperatures, polynomial functions are used. Therefore, the accuracy of the thermocouples is improved, the combined standard uncertainty at 400 °C involve the following uncertainties, at lower temperatures they can be slightly lower.

4.4. Calibration

Several heat transfer correlations, besides the mean overall heat transfer coefficient provided by the manufacturer, have been implemented in the models and compared against data from experimental campaigns. In the shell side: Gaddis and Gnielinski [21], the Bell-Delaware method [25] and a correlation proposed in [26] which is a curve fit from data provided in [27], whereas in the tube side: [28], [29] and [30] correlations have been also tested.

However, simulation results did not agree with experimental data. This is because there is a performance detriment in the heat exchanger [10]. In order to identify the origin of the performance detriment and to develop an accurate heat exchanger model, thermal losses as well as heat transfer correlations on both fluid sides were calibrated against experimental data. The applied methodology is explained in detail in [31].

Heat transfer coefficients can be calculated from the Nusselts number by means of eq. 24,

$$\alpha = Nu\frac{K}{D}. \tag{24}$$

A commonly used expression to calculate the heat transfer coefficient in the shell side of heat exchangers, and analogous to eq. 24, is given by eq. 25,

$$\alpha = \frac{jc_pG}{Pr^{2/3}}. \tag{25}$$

4.4.1. Thermal losses.

As a result of the calibration process using experimental data as described in [31], the following Colburn j factor for thermal losses, eq. 26, was obtained. Therefore, the heat transfer coefficient for thermal losses is calculated by means of eq. 25 and eq. 26. This heat transfer correlation can be used in all the developed models.

$$j_{loss} = 1.1858Re_{loss}^{-0.9545}. \tag{26}$$

4.4.2. Tube-side heat transfer correlation.

The QSS, DY and DYTC models do not model the tube-side inlet and outlet channels in each heat exchanger unit, for this reason correlations in the literature cannot be directly used. For instance, Gnielinski's correlation [28] (see eq. 28) was derived considering fluid flow in straight ducts. Although this correlation is a good approximation for the tube side of heat exchangers, the coefficients appearing on it (1000, 12.7) can be adjusted experimentally, since fluid flow path in heat exchangers is commonly complex. Therefore, those coefficients where calibrated in eq. 27 obtaining (1792, 29.93). The calibration was performed using experimental data and the calibration process is described in [31], as a result the tube-side heat transfer coefficient in the QSS, DY and DYTC models can be calculated by means of eq. 24 and eq. 27.

$$Nu_{tb} = \frac{\frac{f_w}{8}(Re_{tb} - 1792)Pr_{tb}}{1 + 29.93\sqrt{f_w/8}(Pr_{tb}^{2/3} - 1)}\left[1 + \left(\frac{d_w}{l_w}\right)^{2/3}\right]. \tag{27}$$

Since the DYCM model has into account the tube-side inlet and outlet channels in each heat exchanger unit, the calibration of the previously mentioned coefficients yields similar values to the coefficients in the original Gnielinski's correlation. For this reason, the original correlation has been used, eq. 28.

$$Nu_{tb} = \frac{\frac{f_w}{8}(Re_{tb} - 1000)Pr_{tb}}{1 + 12.7\sqrt{f_w/8}(Pr_{tb}^{2/3} - 1)}\left[1 + \left(\frac{d_w}{l_w}\right)^{2/3}\right]. \tag{28}$$

The friction factor (f_w) in both equations has been calculated considering the Filonenko's correlation [32], eq. 29,

$$f_w = (1.82\ln Re_{tb} - 1.64)^{-2}. \tag{29}$$

4.4.3. Shell-side heat transfer correlation.

Shell-side heat transfer correlation was also calibrated for the QSS, DY and DYTC models as described in [31], therefore the shell-side heat transfer coefficient can be calculated by means of eq. 25 and eq. 30.

$$j_{sh} = 3.2470Re_{sh}^{-1.1077}, \tag{30}$$

Even though the DYCM has a different and more complex shell-side model structure, the calibrated coefficients, eq. 31, are similar to those obtained for the other models, eq. 30.

$$j_{sh} = 3.2609Re_{sh}^{-1.1074}. \tag{31}$$

Nevertheless, the calibrated shell-side correlations (eq. 30 and eq. 31) do not agree with correlations in the literature: Gaddis and Gnielinski [21], the Bell-Delaware method [25] and [26], therefore this suggests that the performance detriment must be related to the heat transfer in the shell side.

The most common causes for deterioration in performance of F-shell heat exchangers are thermal leakage or physical leakage due to the longitudinal baffle [33] together with fouling, corrosion, design errors and fabrication issues. Additionally, two potential issues were identified with this heat exchanger, as presented in [9]. One of them is the bypass of molten salt through the drainage channels and the other one is the nitrogen accumulation inside the shell due to the heat exchanger tilt angle. Further investigation and inspection in the physical device is necessary to address the performance issue.

4.5. Experimental validation

In this section data from experimental campaigns is compared against simulation results from the models previously introduced in section 3, three experiments are considered. One of them in steady-state conditions and the two remaining considering transients: replication of cloud disturbances in the solar field and molten salts, as well as thermal oil, mass flow rate steps. Again, the DYCM model has been discretized in 50 CVs, whereas the DY and DYTC models consider 160 CVs.

4.5.1. Steady-state experiment.

A steady-state experiment was performed in the MOSA facility close to nominal operating conditions (see table 1). Figure 15 shows the inlet molten salt and thermal oil mass flow rates in the experiment. All the models were simulated considering the calibrated heat transfer correlations (see section 4.4), for comparison purposes the DYCM model was simulated also considering the overall heat transfer coefficient provided by the manufacturer (DYCM manufacturer), as well as a shell-side heat transfer correlation available in the literature, Gaddis and Gnielinski's correlation [21] (DYCM correlation).

Experimental inlet and simulated outlet molten salt and thermal oil temperatures can be seen in figures 16 and 17, respectively. Table 6 shows the maximum difference between experimental and simulated thermal oil and molten salt temperatures together with the Root Mean Square Error (RMSE) and the execution time for each model. Simulation re-

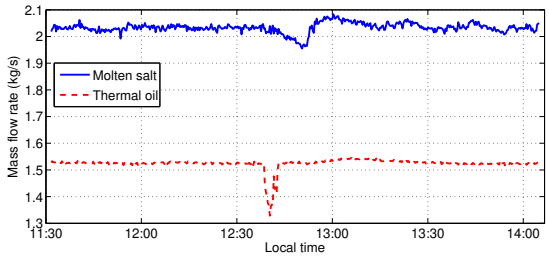

Figure 15: Steady-state experiment: mass flow rates

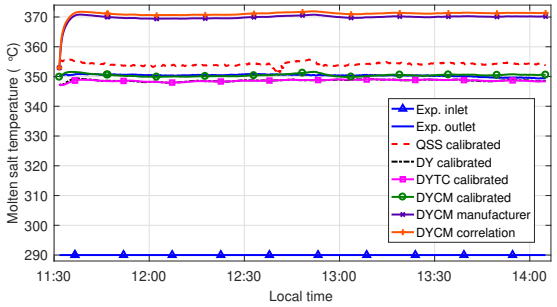

Figure 16: Steady-state experiment: molten salt temperatures

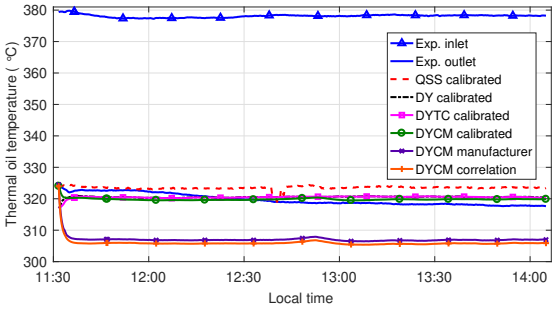

Figure 17: Steady-state experiment: thermal oil temperatures

Table 6: Simulation results in the steady-sate experiment

Model	Molten salt		Thermal oil		Execution time
	Maximum difference	RMSE	Maximum difference	RMSE	
QSS calibrated	5.51 °C	3.87 °C	6.17 °C	4.22 °C	3.06 s
DY calibrated	3.21 °C	1.77 °C	7.25 °C	2.09 °C	12.09 s
DYTC calibrated	3.37 °C	1.80 °C	7.25 °C	2.14 °C	11.60 s
DYCM calibrated	1.22 °C	0.54 °C	3.04 °C	1.78 °C	54.45 s
DYCM manufacturer	20.82 °C	19.56 °C	15.75 °C	12.81 °C	20.03 s
DYCM correlation	22.00 °C	20.73 °C	17.02 °C	13.91 °C	59.57 s

Table 7: Simulation results in the cloud disturbance experiment

Model	Molten salt		Thermal oil		Execution time
	Maximum difference	RMSE	Maximum difference	RMSE	
QSS	13.58 °C	4.30 °C	14.14 °C	6.26 °C	2.94 s
DY	6.70 °C	2.68 °C	12.01 °C	3.76 °C	9.90 s
DYTC	4.28 °C	2.61 °C	10.59 °C	3.35 °C	9.61 s
DYCM	4.29 °C	1.51 °C	9.85 °C	2.68 °C	66.07 s

sults from calibrated models agree with experimental data, being the DYCM results the most precise but at expense of a higher computation time since the DYCM model is more complex than the other models. It can be seen in figures 16 and 17 that for the DYCM manufacturer and DYCM correlation models, the simulated performance is much higher than the real one, this again suggests issues in the shell-side heat transfer of the heat exchanger, as commented in section 4.4.

4.5.2. Cloud disturbance experiment.

Clouds in the solar fields were replicated in an operating mode 3 experiment (see section 2) by reducing the oil heater temperature and then setting it back to its original value, as it can be seen in the thermal oil inlet temperature in figure 19. This figure also shows the experimental and simulated thermal oil outlet temperatures given by each model. Thermal oil and molten salt mass flow rates were kept constant to their nominal values during the whole experiment. It can be seen in figure 19 that the simulated thermal oil outlet temperature given by the models react faster to the disturbance that the real system, this must be further studied and it might be related to unmodeled dynamics or to issues in the thermal oil outlet temperature measurement.

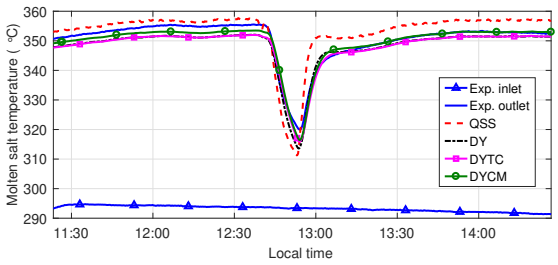

Figure 18: Cloud experiment: molten salt temperatures

On the other hand, figure 18 shows the experimental inlet and outlet as well as simulated outlet molten salt temperatures given by each model. In this case, all the models provides a good agreement with respect to experimental data. This fact reinforces the idea that the disagreement between the reaction time of the real system and the models with respect to the thermal oil outlet temperature should be related to

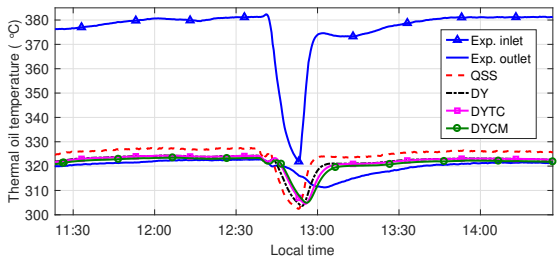

Figure 19: Cloud experiment: thermal oil temperatures

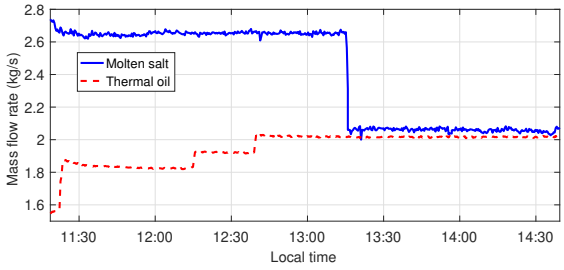

Figure 20: Mass flow rate steps experiment: mass flow rates

issues in the thermocouple, thermowell, or in the piping between the outlet of the heat exchanger and the thermocouple, because otherwise the outlet molten salt dynamics would not show such a good agreement.

Table 7 shows the same information than Table 6 but for the cloud disturbance experiment. It can be seen that the DYCM model provides slightly better results than the DYTC model but at the expense of a much higher computation time.

4.5.3. Mass flow rate experiment.

Some thermal oil and molten salt mass flow rate steps were applied in this experiment as shown in figure 20. Same information as for the previous experiment is also shown in this case, where figure 21 shows the experimental inlet and outlet as well as simulated outlet molten salt temperatures for each model, figure 22 shows same variables for thermal oil and table 8 shows the maximum difference between experimental and simulated thermal oil and molten salt temperature, the RMSE and execution times.

There is a good agreement between experimental and simulated outlet thermal oil and outlet molten salt temperatures, as shown in table 8, being the RMSE lower than 3.50 °C for all the evaluated models. The maximum difference between experimental and simulated temperatures is mainly due to the initialization process, where the DYCM model provides the best initialization as also shown in table 8.

In this experiment, it was found out that the models slightly underpredict heat transfer when the thermal oil mass flow rate is higher than its nominal value while keeping the molten salt mass flow rate at nominal conditions. This is depicted in figure 20, at approximately 13:15, where the thermal oil mass flow rate is 2.02 kg/s, being its nominal value 1.57 kg/s (see table 1), and keeping the molten salt mass flow rate at its nominal value, 2.08 kg/s. Figure 22 shows that heat transfer is slightly underpredicted, since the simulated thermal oil outlet temperatures are higher that the experimental one. In figure 21, this can be also appreciated since simulated molten salt temperatures are lower that the experimental one. Nevertheless, the discrepancy between experimental and simulated temperatures is still low in this part of the experiment, the highest one is found in the thermal oil temperature, being this lower than 2.90 °C for the DY, DYTC and DYCM models, and lower than 3.60 °C for the QSS model. Again the DYCM model provides slightly better results at the expense of a much higher computation time (see table 8).

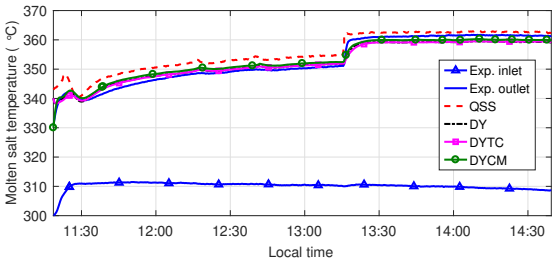

Figure 21: Mass flow rate steps experiment: molten salt temperatures

Table 8: Simulation results in the mass flow rate steps experiment

Model	Molten salt		Thermal oil		Execution time
	Maximum difference	RMSE	Maximum difference	RMSE	
QSS	12.33 °C	3.42 °C	12.35 °C	3.44 °C	2.94 s
DY	9.35 °C	1.74 °C	17.02 °C	2.39 °C	12.96 s
DYTC	9.35 °C	1.72 °C	17.02 °C	2.36 °C	13.22 s
DYCM	3.15 °C	1.59 °C	7.68 °C	2.27 °C	72.30 s

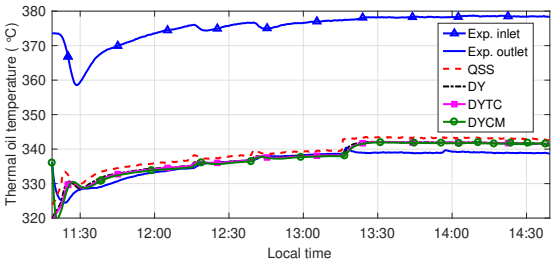

Figure 22: Mass flow rate steps experiment: thermal oil temperatures

5. Conclusions and Ongoing Work

This paper has presented a comparison of different shell-and-tube heat exchanger models with different degree of complexity. Simulations results have been compared against experimental data in terms of accuracy and simulation time. The following paragraphs summarize the main conclusions drawn from this study.

With respect to the tube-side modeling, it is important that the heat exchanger model takes into account the inlet and outlet channels connected to the tube bundle in order to obtain accurate results if heat transfer correlations in the literature for the tube bundle are planning to be used, as it is the case for the DYCM model where the Gnielinski's correlation was considered. Another option is to use general heat exchanger models in the literature and calibrate the tube-side heat transfer correlation, this is the case for the QSS, DY and DYTC models considered in this work, where the tube-side inlet and outlet channels are not taken into account.

All the models helped to identify that there is a performance detriment in the heat exchanger studied, but the most complex model, the DYCM model, suggests that the performance detriment is related to the heat transfer in the shell side, i.e between the shell-side fluid and the tube bundle, since heat transfer correlations in the literature can be used in the tube-side and simulation results agree with experimental data, whereas the shell-side heat transfer correlation had to be calibrated.

According to the results, the QSS is a fast and simple algebraic model which may be used in advanced control techniques which require fast and multiple model evaluations, for instance model predictive control. The DYCM model provides slightly better results with respect to experimental data, however the computation time to perform the simulations is much higher than with the other models; if this simulation time can be assumed, this is the most precise model for process simulations as well as to test control strategies in simulation. The DYTC model provides better results than the QSS and DY models and results are close to those obtained with the DYCM model but in lower computation times.

Ongoing work includes inspecting the real system in order to identify the physical causes for the heat exchanger performance detriment. Additionally, the QSS and DYCM models are being used for the design, testing, validation and optimization of control strategies in heat exchangers for TES systems in solar thermal power plants [34]. In particular, the QSS model is being used in a feed-forward model predictive control and the DYCM model as the dynamic model of the real system.

Acknowledgements

This research has been funded by the EU 7^{th} Framework Programme (Theme Energy 2012.2.5.2) under grant agreement 308912 - HYSOL project - Innovative Configuration of a Fully Renewable Hybrid CSP Plant, the Spanish Ministry of Economy and Competitiveness through ERDF, PLAN E funds (C.N. SolarNOVA ICT-CEPU 2009-02) and the National R+D+i Plan Project DPI2014-56364-C2-1/2-R (ENERPRO-EFFERDESAL).

References

[1] T. Skoglund, K. Arzen, P. Dejmek, Dynamic object-oriented heat exchanger models for simulation of fluid property transitions, International Journal of Heat and Mass Transfer 49 (13-14) (2006) 2291–2303. doi:10.1016/j.ijheatmasstransfer.2005.12.005.

[2] F. Zaversky, M. Sánchez, D. Astrain, Object-oriented modeling for the transient response simulation of multi-pass shell-and-tube heat exchangers as applied in active indirect thermal energy storage systems for concentrated solar power, Energy 65 (2014) 647–664. doi:10.1016/j.energy.2013.11.070.

[3] U. Herrmann, D. W. Kearney, Survey of Thermal Energy Storage for Parabolic Trough Power Plants, Journal of Solar Energy Engineering 124 (2) (2002) 145. doi:10.1115/1.1467601.

[4] S. Relloso, E. Delgado, Experience with molten salt thermal storage in a commercial parabolic trough plant. Andasol-1 commissioning and operation, in: 15^{th} SolarPACES Conference, Berlin, Germany, 2009.

[5] S. Relloso, J. Lata, Molten Salt Thermal Storage: A Proven Solution to increase Plant Dispatchability. Experience in Gemasoalr Tower Plant, in: 17^{th} SolarPACES Conference, Granada, Spain, 2011.

[6] F. Zaversky, M. M. Rodríguez-García, J. García-Barberena, M. Sánchez, D. Astrain, Transient behavior of an active indirect two-tank thermal energy storage system during changes in operating mode - An application of an experimentally validated numerical model, Energy Procedia 49 (2013) 1078–1087. doi:10.1016/j.egypro.2014.03.117.

[7] M.-M. Rodríguez-García, First Experimental Results of a PTC Facility Using Gas as the Heat Transfer Fluid, in: 15^{th} SolarPACES Conference, Berlin, Germany, 2009.

[8] M.-M. Rodríguez-García, E. Zarza, Design and Construction of an Experimental Molten Salt Test Loop, in: 17^{th}SolarPACES Conference, Granada, Spain, 2011.

[9] M.-M. Rodríguez-García, M. Herrador-Moreno, E. Zarza Moya, Lessons learnt during the design, construction and start-up phase of a molten salt testing facility, Applied Thermal Engineering 62 (2) (2014) 520–528. doi:10.1016/j.applthermaleng.2013.09.040.

[10] J. Bonilla, M.-M. Rodríguez-García, L. Roca, L. Valenzuela, Object-Oriented Modeling of a Multi-Pass Shell-and-Tube Heat Exchanger and its Application to Performance Evaluation, in: 1^{st} Conference on Modelling, Identification and Control of Nonlinear Systems (MICNON), Saint-Petersburg, Russia, 2015, pp. 107 – 112.

[11] U. Herrmann, B. Kelly, H. Price, Two-tank molten salt storage for parabolic trough solar power plants, Energy 29 (5-6) (2004) 883–893. doi:10.1016/S0360-5442(03)00193-2.

[12] Modelica Association, Modelica Standard Library 3.2.1 (2013).
URL http://www.modelica.org

[13] F. Casella, M. Otter, K. Proelss, C. Richter, H. Tummescheit, The Modelica Fluid and Media library for modeling of incompressible and compressible thermo-fluid pipe networks, in: Proc. 5^{th} International Modelica Conference, Vienna, Austria, 2006, pp. 631–640.

[14] A. B. Zavoico, Solar Power Tower - Design Basis Document, Tech. Rep. SAND2001-2100, Sandia National Laboratories, Albuquerque, USA (2001).

[15] R. Ferri, A. Cammi, D. Mazzei, Molten salt mixture properties in RELAP5 code for thermodynamic solar applications, International Journal of Thermal Sciences 47 (12) (2008) 1676–1687. doi:10.1016/j.ijthermalsci.2008.01.007.

[16] Solutia, Therminol VP-1 heat transfer fluid - Vapour and Liquid phases, Technical bulletin 7239115C (2008).

[17] Z. S. Spakovszky, Unified: Thermodynamics and Propulsion (2008).
URL http://web.mit.edu/16.unified/www/FALL/thermodynamics/notes/

[18] D. J. Correa, J. L. Marchetti, Dynamic Simulation of Shell-and-Tube Heat Exchangers, Heat Transfer Engineering 8 (1) (1987) 50 – 59. doi:10.1080/01457638708962787.

[19] S. Patankar, Numerical Heat Transfer and Fluid Flow, Hemisphere, Washington D.C, 1980.

[20] S. Gaddis, Pressure drop on the shell side of shell-and-tube heat exchangers with segmental baffles 36 (1997) 149–159. doi:10.1016/S0255-2701(96)04194-3.

[21] VDI, VDI Heat Atlas, 2nd Edition, Springer, 2010.

[22] L. Moody, Friction factors for pipe flow, Transactions of the ASME 66 (1944) 671–684.

[23] Dassault Systemes, Dymola 2015 - Multi-Engineering Modeling and Simulation (2015).
URL http://www.dymola.com

[24] L. Petzold, A description of DASSL: a Diferential/Algebraic System Solver, Scientific Computing (1983) 65–68.

[25] K. Thulukkanam, Shell and Tube Heat Exchanger Design, in: Heat Exchanger Design Handbook, Second Edition, Dekker Mechanical Engineering, CRC Press, 2013, pp. 237–336. doi:doi:10.1201/b14877-6.

[26] R. W. Serth, Process Heat Transfer: Principles and Applications, Elsevier Science, 2007.

[27] A. D. Kraus, A. Aziz, J. Welty, Extended Surface Heat Transfer, Wiley, 2002.

[28] V. Gnielinski, New equations for heat and mass transfer in turbulent pipe flow and channel flow, International Chemical Engineering 2 (16) (1976) 359–368.

[29] F. W. Dittus, L. M. K. Boelter, Heat transfer in automobile radiators of the tubular type, University of California Publications in Engineering 2 (1) (1930) 443–461. doi:10.1016/0735-1933(85)90003-X.

[30] H. Hausen, Darstellung des Wärmeüberganges in Rohren durch verallgemeinerte Potenzbeziehyngen, VDI - Verfahrenstechnik 4 (1943) 91–98.

[31] J. Bonilla, A. de la Calle, M.-M. Rodríguez-García, L. Roca, L. Valenzuela, Experimental Calibration of Heat Transfer and Thermal Losses in a Shell-and-Tube Heat Exchanger, in: Proc. 11^{th} International Modelica Conference, Versailles, France, 2015.

[32] G. K. Filonenko, Hydraulic drag in pipes, Teploenergetika 1 (4) (1954) 40 – 44.

[33] R. Mukherjee, Does Your Application Call for an F-Shell Heat Exchanger?, CEP magazine (April) (2004) 40–45.

[34] L. Roca, J. Bonilla, M.-M. Rodríguez-García, P. Palenzuela, A. De La Calle, L. Valenzuela, Control strategies in a thermal oil - Molten salt heat exchanger, AIP Conference Proceedings 1734 (2016) 130017–1–130017–8. doi:10.1063/1.4949227.